Isoelectronic Tungsten Doping in Monolayer $MoSe_2$ for Carrier Type Modulation

*Xufan Li, Ming-Wei Lin, Leonardo Basile, Saban M. Hus, Alexander A. Puretzky, Jaekwang Lee, Yen-Chien Kuo, Lo-Yueh Chang, Kai Wang, Juan C. Idrobo, An-Ping Li, Chia-Hao Chen, Christopher M. Rouleau, David B. Geohegan, and Kai Xiao**

2D transition metal dichalcogenides (TMDs) have emerged as new promising materials for the next generation of electronics and optoelectronics based on atomically thin systems.[1–3] They show excellent optical, electronic, and optoelectronic properties such as highly efficient light harvesting,[4] highly sensitive photodetection,[3] and low-threshold lasing.[5] To tune the properties of TMDs and realize their potential applications, band structure engineering is of great importance. For example, a wide range of bandgap values can be obtained to match the solar spectrum[6–9] for solar energy conversion.[4,10] Band structure engineering can also effectively modulate the carrier type of semiconducting TMDs[11–14] for field-effect transistors (FETs) and p–n junctions, which are highly desirable for integrated electronics.

Doping is one of the most effective ways to engineer the band structure of a material to precisely tailor its properties for desired applications. Due to spatial confinement, doping in 2D TMDs produces especially pronounced effects.[6–17] Diverse doping strategies for 2D TMDs have so far been developed, including direct charge injection via electrostatic FET gating,[11] the donation of charge from physically adsorbed volatile molecules[15] or alkali metals,[16] and approaches involving covalent bonding via edge functionalization[9,14] or substituted atoms.[12,13,18,19] Of these methods, substitutional doping via covalent bonding with different metal or chalcogen atoms is highly desirable in order to produce robust, stable alloys.[12,13]

Dr. X. Li, Dr. M.-W. Lin, Dr. S. M. Hus,
Dr. A. A. Puretzky, Dr. K.Wang, Dr. J. C. Idrobo,
Dr. A.-P. Li, Dr. C. M. Rouleau, Dr. D. B. Geohegan,
Dr. K. Xiao
Center for Nanophase Materials Sciences
Oak Ridge National Laboratory
Oak Ridge, TN 37831, USA
E-mail: xiaok@ornl.gov
Dr. L. Basile
Departamento de Física
Escuela Politécnica Nacional
Quito 17012759, Ecuador
Dr. J. Lee
Department of Physics
Pusan National University
Busan 609-735, South Korea
Dr. Y.-C. Kuo, Dr. L.-Y. Chang, Dr. C.-H. Chen
National Synchrotron Radiation Research Center (NSRRC)
Hsinchu 30076, Taiwan

DOI: 10.1002/adma.201601991

The substitutional doping of electron-rich or hole-rich atoms into the lattice of 2D TMDs follows the conventional band structure engineering approach to tune the bandgap and modulate the free carrier type in semiconductors. For example, recently the electrical conduction in monolayer MoS_2 has been modulated by substitution of Mo atoms with electron-donor atoms such as Re (n-type)[20] and hole-donors such as Nb (p-type).[12,13] However, in these cases when the size difference between the dopant and host atoms becomes too large, unintended effects such as incorporation of impurities or dislocations in the lattice[21] can occur and the solubility of the dopant atoms becomes hard to control.

Alternatively, these drawbacks can be suppressed by isoelectronic doping with dopant atoms similar to those of the host. Isoelectronic dopants tend to more easily form alloys, impede the generation and multiplication of dislocations, and reduce the formation of amphoteric native defects.[22] Although isoelectronic dopants provide no extra electrons or holes, it is possible that their different electronegativity can introduce trapping potentials in the lattice to modulate the free carrier density and net conductivity behavior.

So far, two types of 2D TMD isoelectronic alloys have been synthesized by substituting either isoelectronic chalcogens, e.g., $MoS_{2(1-x)}Se_{2x}$ (refs. [6–8]), or transition metals, e.g., $Mo_xW_{1-x}S_2$ (refs. [18,23–25]). These isoelectronic alloys show a continuous variation of bandgap energy, resulting in photoluminescence (PL) with tunable emission wavelength in a wide spectral range.[6–8,18,23] A major difference between the chalcogen and metal isoelectronic alloys is that the strong spin–orbit coupling resulting from the d-orbitals of the transition metals in TMDs can lead to large valence band splittings of several hundreds of meV,[19] which can be exploited in the metal alloys (e.g., $Mo_{1-x}W_xSe_2$) to tune the degree of spin or valley polarization.

However, the tuning of electrical properties (such as the carrier type) in isoelectronic 2D TMD alloys has never been demonstrated. As has been widely reported, monolayer $MoSe_2$ is natively n-doped[26] and WSe_2 is intrinsically p-type doped,[27,28] although the characteristics may vary with substrates or contact metals.[29] Since Mo and W have different d-orbital band energies, and the band edges of $MoSe_2$ and WSe_2 are mainly determined by the contributions from these d-orbitals, it is reasonable to expect that without changing the fundamental band structure, 2D TMD alloys and homojunctions based on isoelectronic substitution in the $MoSe_2$–WSe_2 system should provide uniform alloys with tunable band edge position, and a modulation between p- or n-type doping. Monolayer $Mo_{1-x}W_xSe_2$

should therefore be a promising candidate for electrical carrier type modulation. According to theoretical predictions, monolayer $Mo_{1-x}W_xSe_2$ alloys should be thermodynamically stable and direct bandgap semiconductors.[30,31] Especially, the formation energies for $Mo_{1-x}W_xSe_2$ alloys are negative due to well-matched lattice constants, similar electronic structures, and increased attractive Coulomb interaction (caused by different atomic orbital energy and electronegativity of Mo and W) between $MoSe_2$ and WSe_2,[30,31] which means that $Mo_{1-x}W_xSe_2$ alloy formation is energetically favorable. Until now 2D $Mo_{1-x}W_xSe_2$ alloys have only been fabricated by mechanical exfoliation.[32]

In this study, a chemical vapor deposition (CVD) method was employed to synthesize semiconducting $Mo_{1-x}W_xSe_2$ alloy monolayers with x ranging from 0 to ≈0.18. Atomic-resolution STEM imaging, Auger electron and spectroscopic characterizations showed that the W atoms uniformly incorporate into the monolayer $MoSe_2$ lattice by substitution of Mo, forming ideal random alloys with significantly enhanced photoluminescence. For the first time it was demonstrated that isoelectronic doping of W into $MoSe_2$ switches the dominant conduction type of the monolayer flakes, suppressing n-type conduction in monolayer $MoSe_2$ and tunably enhancing p-type conduction to become dominant at increased W concentration. Localized "W-rich" regions in the $Mo_{1-x}W_xSe_2$ lattice were revealed, where the valence band maximum (VBM) shifts toward the Fermi level, resulting in p-type nondegenerate doping in $Mo_{1-x}W_xSe_2$ monolayers. Vertically stacked monolayers of p-type $Mo_{1-x}W_xSe_2$ and n-type $MoSe_2$ were used to fabricate van der Waals (vdW) p–n homojunctions to demonstrate their applicability for gate-tunable current rectification. Such tunable n- and p-type conduction realized within an isoelectronic monolayer alloy is highly encouraging as an important new strategy to synthetically adjust the functionality of 2D TMD systems for many electronic and optoelectronic applications.

Monolayer $MoSe_2$ crystals were synthesized through a low pressure CVD method similar to those described elsewhere,[7] in which Se powder was used to react with MoO_3 in the presence of hydrogen gas. $Mo_{1-x}W_xSe_2$ was obtained by mixing WO_3 and MoO_3 at different ratios as the source materials (see the Supporting Information for details of the synthesis process). **Figure 1**a,b shows optical micrographs of $MoSe_2$ flakes grown on SiO_2 (250 nm)/Si and fused quartz substrates, respectively. Individual flakes are triangular in shape with the size ranging from tens to hundreds of microns. $Mo_{1-x}W_xSe_2$ flakes show similar triangular shapes and sizes (Figure S1, Supporting Information). Atomic force microscopy (AFM) analyses indicate that the thickness of each individual flake is ≈0.7 nm (Figures 1c), corresponding to monolayer $MoSe_2$ and $Mo_{1-x}W_xSe_2$. Both optical microscopy and AFM characterization demonstrated that large-size, uniform monolayer crystals of both $MoSe_2$ and $Mo_{1-x}W_xSe_2$ were synthesized and, by tuning the growth conditions, the size, layer number, and density of the flakes were controlled (Figure S1, Supporting Information). Micro-X-ray photoelectron spectroscopy measurements[33] confirmed the existence of W^{4+} in the $Mo_{1-x}W_xSe_2$ flakes (Figure S2, Supporting Information). Figure 1e shows a scanning electron microscopy (SEM) image of a monolayer $Mo_{1-x}W_xSe_2$. Nano-Auger elemental mapping revealed that the Mo, W, and Se compositions are uniform over the $Mo_{1-x}W_xSe_2$ flake (Figure 1e,f; see Figure S3 in the Supporting Information for the Auger elemental mapping of monolayer $MoSe_2$), with the W concentration of 0.18 ± 0.02 (≈18%). The W concentration in monolayer $Mo_{1-x}W_xSe_2$ was tuned by altering the amount of WO_3 in the source. In this report, we focus on three typical concentrations: ≈2%, ≈7%, and ≈18% (i.e., x = 0.02, 0.07, and 0.18, respectively), obtained with the weight ratio of MoO_3/WO_3 being ≈1/0.05, ≈1/0.1, and ≈1/1, respectively.

The atomic structures of $MoSe_2$ and $Mo_{1-x}W_xSe_2$ monolayers were investigated using annular dark field (ADF) imaging on an aberration-corrected scanning transmission electron microscope (STEM). As revealed by the atomic resolution ADF image in Figure 1g, a $MoSe_2$ monolayer displays a honeycomb structure composed of alternating brighter and dimmer atomic sites. The intensity line profile along the solid green line is shown in Figure 1i (lower row). As the ADF-STEM image is Z-contrast, the image intensity depends on the total atomic number of the atoms occupying each site. According to the corresponding simulated ADF-STEM image (Figure 1h) and line profiles (Figure 1i, upper row), the brighter sites correspond to columns occupied by two Se atoms while each dimmer site contains one Mo atom, which is in good agreement with the experimental STEM images.

Figure 1j shows the ADF-STEM image of monolayer $Mo_{0.82}W_{0.18}Se_2$, in which the same honeycomb atomic structure as that corresponding to the $MoSe_2$ monolayer is displayed. A portion of the Mo sites show brighter contrast as indicated by the intensity line profile in Figure 1l (lower row). These sites correspond to W atoms, as confirmed by the simulated ADF-STEM image (Figure 1k) and the corresponding intensity line profile (Figure 1l, upper row). The ADF-STEM results demonstrate that W atoms substitute for Mo in the honeycomb lattice, and no interstitial atom is observed (Figure 1j; Figure S4, Supporting Information). Statistical analysis of the ADF-STEM image in Figure 1j and a lower magnified image in Figure S4 (Supporting Information) estimates that W atoms in monolayer $Mo_{0.82}W_{0.18}Se_2$ substitute for ≈18% of the Mo sites, which is in good agreement with the Auger analysis. The alloying degrees (describing the extent of alloying[34]) of W and Mo were calculated to be 99.2% and 98.2 % (the calculation method was described in ref. [24] and [33]), respectively, very close to 100%, indicating that this $Mo_{1-x}W_xSe_2$ is close to an ideal random alloy.[34] No indication of phase separation is found. This experimental observation agrees well with the theoretical prediction that the formation energy of Mo-W alloys is negative,[30] indicating that $Mo_{1-x}W_xSe_2$ tends to form random alloys, rather than segregate into a lateral heterostructure of $MoSe_2$–WSe_2. It is worth noticing that at the atomic scale (Figure 1j,k; Figure S4, Supporting Information) there are some regions with higher W concentration in the $Mo_{1-x}W_xSe_2$ lattice, forming "W-rich" regions. These "W-rich" regions may contribute to the formation of different band structures and may also affect electrical properties of these monolayers, which will be discussed later. We also notice that few Se vacancies exist in the lattice of both $MoSe_2$ and $Mo_{1-x}W_xSe_2$ monolayers (as pointed out by the red arrows in Figure 1g,j). The possible creation of chalcogenide vacancies in monolayer crystals during the growth has been previously reported.[35,36] However, it should be pointed

Adv. Mater. 2016,
DOI: 10.1002/adma.201601991

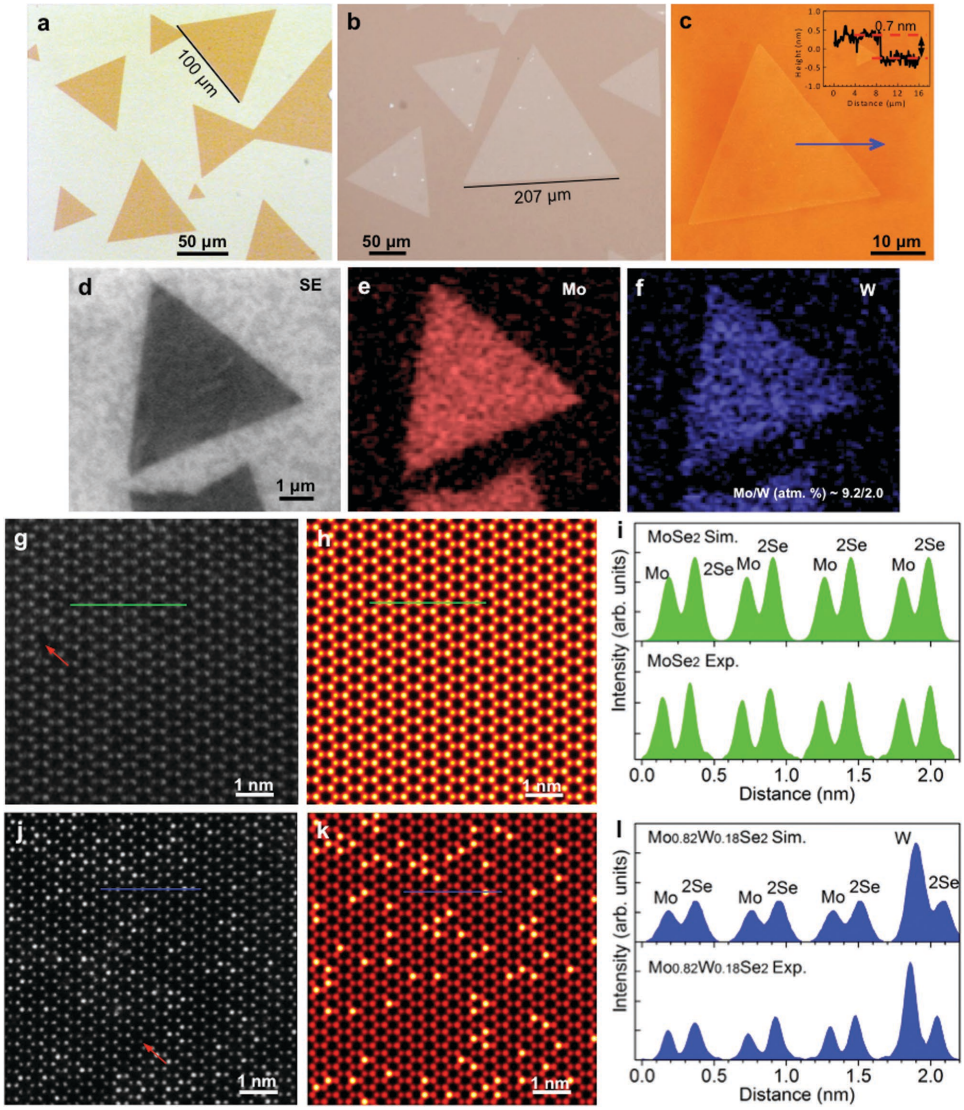

Figure 1. a,b) Optical micrographs of $MoSe_2$ monolayers grown on SiO_2/Si and fused quartz substrates, respectively. c) AFM image of a $Mo_{1-x}W_xSe_2$ monolayer. Inset is the height profile along the solid blue arrow. d) SEM image of a $Mo_{1-x}W_xSe_2$ monolayer. e,f) Nano-Auger elemental mappings of Mo and W on the monolayer shown in (d). The concentration of W is ≈18%. g,h) Experimental (g) and simulated (h) atomic resolution ADF-STEM image of monolayer $MoSe_2$. i) Experimental (Exp., lower row) and simulated (Sim., upper row) intensity line profiles along the solid green line in (g) and (h). j,k) Experimental (j) and simulated (k) atomic resolution ADF-STEM image of monolayer $Mo_{0.82}W_{0.18}Se_2$. The brightest spots correspond to sites where W substitutes Mo. l) Experimental (lower row) and simulated (upper row) intensity line profiles along solid blue line in the (j) and (k). The red arrows in (g) and (j) indicate Se vacancies.

out that these vacancies cannot be used as a doping strategy since they produce deep trap states in TMD monolayers.[35,36] Therefore, the modulation of electrical properties in monolayer $Mo_{1-x}W_xSe_2$ discussed below is not likely to be achieved through the Se vacancies.

The optical properties of $MoSe_2$ and $Mo_{1-x}W_xSe_2$ monolayers were studied using Raman and PL spectroscopy at room temperature, using a 532 nm laser as the excitation source. **Figure 2**a shows the Raman spectra of as-grown monolayer $MoSe_2$ (solid black curve) and $Mo_{0.82}W_{0.18}Se_2$ (solid red curve). Both spectra exhibit three typical Raman modes, i.e., the dominant out-of-plane A_{1g} mode, and the weak in-plane E_{1g} and E^1_{2g} modes.[22] The A_{1g} mode of monolayer $MoSe_2$ peaks at 240.4 cm^{-1}, which is blueshifted to 242.7 cm^{-1} in monolayer $Mo_{0.82}W_{0.18}Se_2$ due to phonon hardening by W-substitution,[37] while the E_{1g} and E^1_{2g} modes do not show an obvious shift between the two monolayer crystals, which are located at 145.7 and 286.8 cm^{-1}, respectively (Figure 2a). Figure 2b shows the room temperature PL spectra of monolayer $MoSe_2$ and three $Mo_{1-x}W_xSe_2$ monolayers with different W concentrations, i.e., x = 0.02, 0.07, and 0.18. The monolayer $MoSe_2$ exhibits a single emission peak at ≈1.529 eV (811 nm, Figure 2b, solid black curve), corresponding to the radiative recombination of the A-exciton (ref. [36]). The A-exciton emission band is greatly enhanced and slightly blueshifted as the W concentration increases, i.e., it is shifted to ≈1.536 eV (807 nm) for the $Mo_{0.82}W_{0.18}Se_2$ monolayer (Figure 2b, solid red

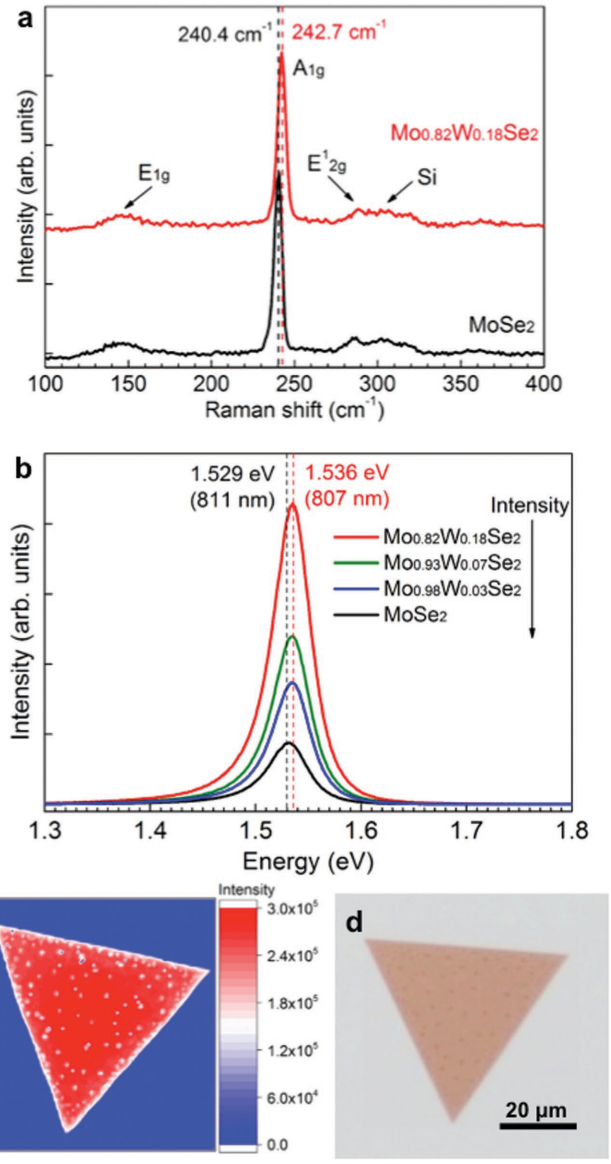

Figure 2. a) Raman spectra of monolayer $MoSe_2$ (solid black curve) and $Mo_{0.82}W_{0.18}Se_2$ (solid red curve) with 532 nm laser excitation. Note that the spectra were offset for clarity. b) PL spectra of monolayer $MoSe_2$ (solid black curve), $Mo_{0.98}W_{0.02}Se_2$ (solid blue curve), $Mo_{0.93}W_{0.07}Se_2$ (solid green curve), and $Mo_{0.82}W_{0.18}Se_2$ (solid red curve) with 532 nm laser excitation. c) PL mapping by integration of intensity from 1.4 to 1.65 eV for a monolayer $Mo_{0.82}W_{0.18}Se_2$ flake. d) Optical micrograph of the flake for PL mapping.

curve). The PL mapping of a monolayer $Mo_{0.82}W_{0.18}Se_2$ flake (Figure 2c, the corresponding optical micrograph is shown in Figure 2d) shows uniform PL across the flake, indicating good crystalline quality and further confirming the uniform distribution of W across the monolayer. The PL results indicate that in monolayer $MoSe_2$ the substitution of up to ≈18% Mo atoms with W does not lead to a significant bandgap energy shift, which is consistent with theoretical calculations on the bandgap structure of monolayer $Mo_{1-x}W_xSe_2$ alloys.[30,31,38] According to the density function theory (DFT) calculations,

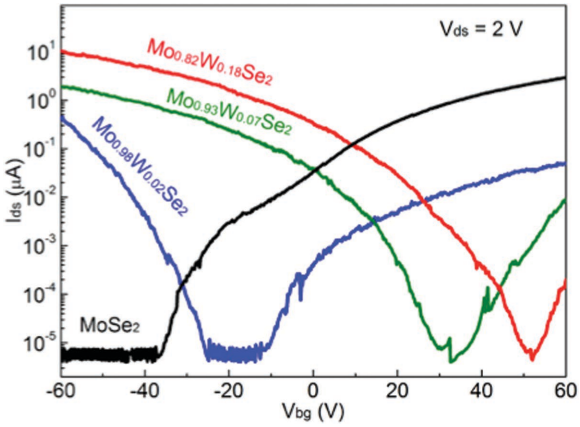

Figure 3. Transfer curves (at $V_{ds} = 2$ V) of FET based on monolayer $MoSe_2$ (solid black curve) and $Mo_{1-x}W_xSe_2$ with different W concentrations (solid blue, green and red curves for $x = 0.02$, 0.07, and 0.18, respectively).

monolayer $Mo_{1-x}W_xSe_2$ with $x < 0.25$ does not show significant changes in electronic bandgaps due to a bowing effect in alloys.[31,38] Therefore, the above results on PL indicate that the optical bandgap of monolayer $Mo_{1-x}W_xSe_2$ is not significantly influenced by the W concentration within the doping (or substitution) limit (≈18%) used in our experiment. However, the PL intensity is greatly enhanced as W is incorporated in $MoSe_2$, which could be due to the suppression of deep level defects that serve as nonradiative recombination centers through isoelectronic doping.[30,39] It corresponds to the technique in traditional light-emitting semiconductors, in which isoelectronic doping was used to greatly increase the luminescence efficiency in those semiconductors.[39]

In order to study the effect of W doping on the electrical properties of monolayer $MoSe_2$, FET devices based on the $MoSe_2$ and $Mo_{1-x}W_xSe_2$ monolayers with different W concentrations were fabricated by patterning source-drain contacts (Ti/Au) on the monolayers while using heavily doped Si substrates as back-gates. **Figure 3** displays the characteristic transfer (I_{ds}–V_{bg}) curves of the monolayer $MoSe_2$ and $Mo_{1-x}W_xSe_2$ FETs with different W concentrations (x = 0.02, 0.07, and 0.18) at room temperature. The output (I_{ds}–V_{ds}) curves of the FETs are shown in Figure S5 (Supporting Information). The monolayer $MoSe_2$ exhibits n-type behavior with an on-off ratio exceeding five orders of magnitude and an electron field-effect mobility (μ_e) of 1.46 $cm^2\ V^{-1}\ s^{-1}$, while the $Mo_{0.82}W_{0.18}Se_2$ shows p-type behavior with a hole mobility (μ_h) of 1.60 $cm^2\ V^{-1}\ s^{-1}$. It is clearly demonstrated that with W doping Mo in monolayer $MoSe_2$, the n-type characteristics of the $MoSe_2$ are suppressed and the p-type characteristics are gradually enhanced with increased hole mobility as the W concentration increases (Figure 3 and **Table 1**). Meanwhile the threshold voltages are shifted from 18 V for $MoSe_2$ to −12 V for $Mo_{0.82}W_{0.18}Se_2$ (Figure 3 and Table 1). For monolayer $Mo_{1-x}W_xSe_2$, a positive shift in the p-type threshold voltage (pV_{th}) from −47.67, −18.33, to −12 V was observed as the W concentration increased from 2%, 7% to 18% (Table 1). This indicates that higher W concentrations in the lattice gradually convert an n-type of carrier to p-type. The doping concentrations (n) of the monolayer $MoSe_2$ and $Mo_{1-x}W_xSe_2$ were calculated according to the equation:

Adv. Mater. 2016,
DOI: 10.1002/adma.201601991

Table 1. Electrical properties of the FET devices made on monolayer $MoSe_2$ and $Mo_{1-x}W_xSe_2$.

	μ_e [$cm^2\ V^{-1}\ s^{-1}$]	μ_h [$cm^2\ V^{-1}\ s^{-1}$]	n_e [cm^{-2}]	n_h [cm^{-2}]	nV_{th} [V]	pV_{th} [V][a)]
$MoSe_2$	1.46	–	3.94×10^{11}	–	18	–
$Mo_{0.98}W_{0.02}Se_2$	0.1	0.16	6.78×10^{10}	1.46×10^{11}	30	–47.67
$Mo_{0.93}W_{0.07}Se_2$	–	1.54	–	4.1×10^{11}	–	–18.33
$Mo_{0.82}W_{0.18}Se_2$	–	1.60	–	4.0×10^{11}	–	–12.0

[a)] μ_e: FET electron mobility, μ_h: FET hole mobility, n_e: electron doping concentration, n_h: hole doping concentration, nV_{th}: n-type conduction threshold voltage, pV_{th}: p-type conduction threshold voltage.

$n = I_{ds}L/qW\mu V_{ds}$, in which q is the electron charge, I_{ds} and V_{ds} are the source-drain current and voltage, respectively, L and W are the length and width of channel, and μ is the field-effect mobility. As listed in Table 1, the hole doping concentration (n_h) increases from 1.46×10^{11} to 4.0×10^{11} cm^{-2} as W concentration increases from 2% to 18%, consistent with the rising trend of V_{th} value. It should be noted that the FET devices with Ti/Au electrodes show high contact resistance (Figure S5, Supporting Information), and therefore the carrier concentration could be underestimated by using the equation: $n = I_{ds}L/qW\mu V_{ds}$.[13] Since the contact issue is similar for all of our devices, the relative trend of electron and hole doping concentrations in $MoSe_2$ and $Mo_{1-x}W_xSe_2$ with different W concentrations should not be affected. It is noticed that some previously reported 2D TMDs doped with nonisoelectronic dopants have very high electron or hole doping concentrations, i.e., $\approx 1.0 \times 10^{13}$ cm^{-2} for potassium-doped MoS_2 (ref. [16]) and $\approx 2.8 \times 10^{14}$ cm^{-2} for Nb-doped MoS_2 (ref. [13]), which belong to degenerate doping and show near-metallic behaviors. In comparison, the much less doping concentration (from 1.46×10^{11} to 4.0×10^{11} cm^{-2}) makes the $Mo_{1-x}W_xSe_2$ doped nondegenerately. It means that isoelectronic doping with W in monolayer $Mo_{1-x}W_xSe_2$ alloys effectively modulates the carrier type without changing the semiconducting characteristic of the flakes.

The carrier type transition in monolayer $MoSe_2$ and $Mo_{1-x}W_xSe_2$ was further investigated by studying the electronic structures using scanning tunneling microscopy and spectroscopy (STM/S) and μ-XPS. The $MoSe_2$ and $Mo_{1-x}W_xSe_2$ monolayers for the STM/S measurements were directly grown on highly ordered pyrolytic graphite (Figure S6, Supporting Information). **Figure 4**a,b shows STM images of monolayer $Mo_{0.82}W_{0.18}Se_2$ under negative (–1 V) and positive (1 V) bias voltages, respectively. Interestingly, bias-dependent features are observed on the flakes, which appear as bright spots with diameters of ≈2 nm under –1 V and become dark spots under 1 V, as indicated by solid white arrows in Figure 4a,b. These features are not observed on monolayer $MoSe_2$, which is generally "clean" under different bias conditions (Figure S7, Supporting Information). These spots are thus likely related to the W doping. Figure 4c,d shows high-magnification STM images (under –1 V) of monolayer $Mo_{0.82}W_{0.18}Se_2$, featuring the atomic

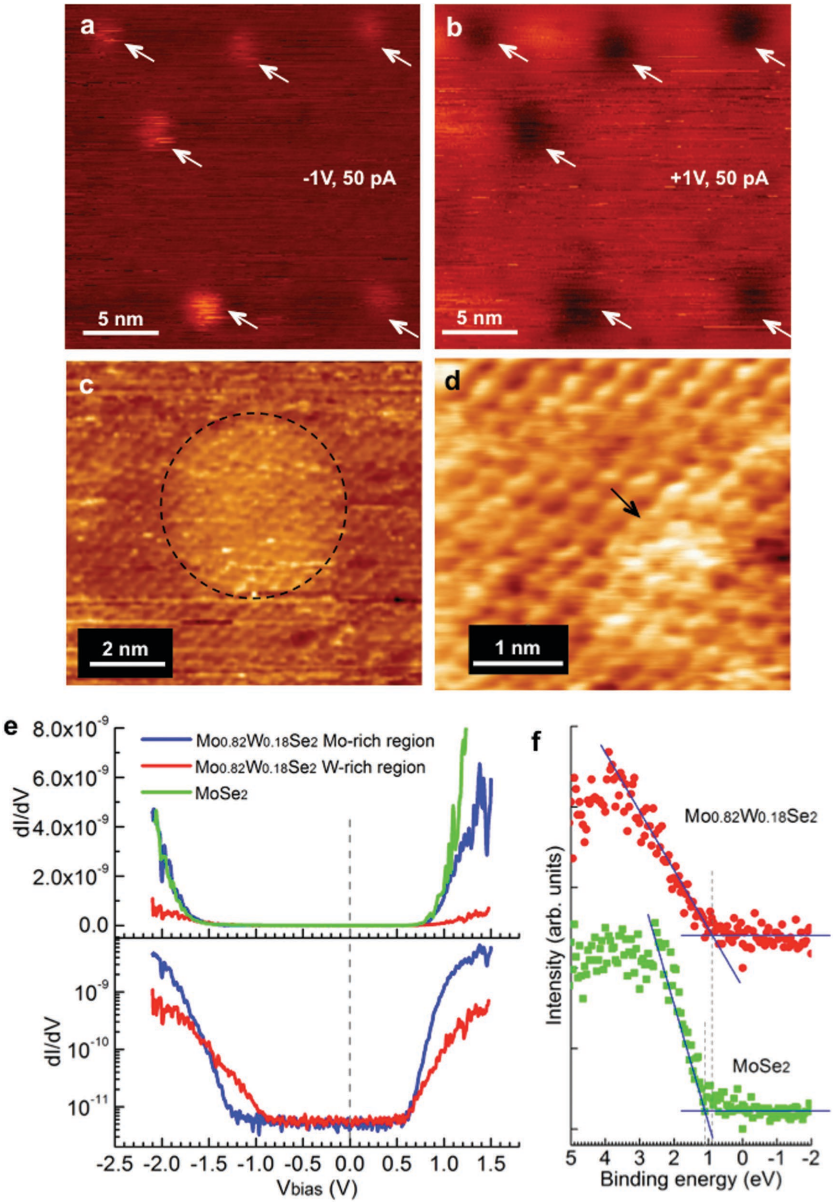

Figure 4. a,b) Low magnification STM images obtained from $Mo_{0.82}W_{0.18}Se_2$ with a) $V = -1$ V, $I = 50$ pA and b) $V = 1$ V, $I = 50$ pA. The solid white arrows indicate bias-dependent features. c,d) High magnification STM images obtained from $Mo_{0.82}W_{0.18}Se_2$ with $V = -1$ V, $I = 50$ pA. e) STS dI/dV–V spectra obtained from monolayer $MoSe_2$ (solid green curve), and the "Mo-rich" region (solid blue curve) and the "W-rich" region (solid red curve) in monolayer $Mo_{0.82}W_{0.18}Se_2$. The dI/dV is plotted in both linear (up) and logarithmic scale (down). f) XPS spectra showing the VBM of $MoSe_2$ (green squares) and $Mo_{0.82}W_{0.18}Se_2$ (red dots). The spectra were obtained using synchrotron micro-X-ray from flakes shown in Figure S2 (Supporting Information).

structures of the "clean" region and a bright region (indicated by the dashed black circle in Figure 4c) with lower contrast compared to the ones in Figure 4a. Both regions show similar hexagonal lattice of monolayer $MoSe_2$ and $Mo_{1-x}W_xSe_2$, which confirms that the bright region retains the lattice integrity of monolayer crystals. The atoms appearing bright under −1 V are W atoms (as indicated by the black arrow in Figure 4d) because the local density of states near the VBM is localized at W sites, and instead at Mo sites near the conduction band minimum (CBM) as indicated by theoretical calculation.[25,30,38] It is shown in Figure 4c that the density of W atoms in the "clean" region is lower than that in the bright spot. By relating to the ADF-STEM results (Figure 1g), the bright spots shown in STM images (under −1 V) are actually the "W-rich" regions. Therefore, we denote the bias-dependent spots shown in Figure 4a,b as "W-rich" regions and the "clean" region as the "Mo-rich" region. It should be noted that the variation in contrast between the "W-rich" region as shown in Figure 4a,c is likely to result from the difference in the number of W atoms and their arrangements in these regions.

To examine the electronic structures, STS dI/dV–V spectra were acquired from the monolayer $MoSe_2$, as well as from the "W-rich" and "Mo-rich" regions in monolayer $Mo_{0.82}W_{0.18}Se_2$, as shown by the solid green, blue, and red curves, respectively, in Figure 4e. The bandgap of monolayer $MoSe_2$ is estimated to be ≈1.85 eV (Figure 4e, green curve), similar to the STS results reported previously.[40] The difference between the electronic bandgap measured from STS and the optical bandgap measured from PL is indicative of the strong exciton binding energy of 0.32 eV. The dI/dV–V spectrum from the "Mo-rich" region in the $Mo_{0.82}W_{0.18}Se_2$ (Figure 4e, blue curve) is similar to that from the $MoSe_2$. However, in the "W-rich" regions, the K point of the VBM shifts toward the Fermi level for ≈0.36 eV compared with the "Mo-rich" region, although the locations of CBM are close to each other (Figure 4e, lower row). It can also be seen that the dI/dV value of the "W-rich" regions is higher than that of the "Mo-rich" region at −1 V bias, but becomes lower at +1 V bias, which is in agreement with the STM images in Figure 4a,b. Previous DFT calculations[38] showed that the CBM states are strongly localized around the d_z^2 orbitals of the Mo atoms in $Mo_{1-x}W_xSe_2$, whereas the VBM is more uniformly contributed by the d_{xy} and $d_{x^2-y^2}$ orbitals of both Mo and W atoms. As a result, a small amount of W incorporated into $MoSe_2$ does not affect the CBM of alloys, but the VBM energy varies with the W composition due to the in-plane orbital coupling, which delocalizes the wavefunction. Therefore, substitution of Mo with W in $MoSe_2$ will reduce electron attraction strength of Mo due to the smaller electron affinity of Mo (0.7473 eV) than that of W (0.8163 eV), and shift the VBM to the Fermi level.

In order to further verify the contribution of the localized and randomly distributed "W-rich" regions to electronic structure of the monolayer $Mo_{1-x}W_xSe_2$ at the macroscopic scale, XPS spectra were also measured. The VBM of monolayer $MoSe_2$ and $Mo_{0.82}W_{0.18}Se_2$, obtained by extrapolation of the linear region in the XPS spectra shown in Figure 4f, is located at ≈1.1 and ≈0.9 eV below the Fermi level, respectively. The fact that $Mo_{0.82}W_{0.18}Se_2$ shows a VBM closer to the Fermi level (by ≈0.2 eV) indicates that the $Mo_{0.82}W_{0.18}Se_2$ is more favorable for p-type doping. Therefore, the XPS results are in good agreement with the STS observations that imply that the VBM shift toward the Fermi level upon W substitution resulting in p-type doping in monolayer $Mo_{1-x}W_xSe_2$.

With both n-type $MoSe_2$ and p-type $Mo_{1-x}W_xSe_2$, we explored the fabrication and properties of an atomically thin p–n homojunction. Note that this junction should be considered as a homojunction due to the fact that the band structure of monolayer $Mo_{1-x}W_xSe_2$ with $0<x<0.18$ is very similar to that of monolayer $MoSe_2$ (Figure 2b).[13,30] The diode characteristics expected for such a homojunction interface, due to the similar band structures, should result in fewer carrier trap sites than encountered for heterojunctions, leading to more efficient current rectification and photovoltaic response.[13] Monolayer $MoSe_2$ flakes were transferred from the substrate and stacked on monolayer $Mo_{1-x}W_xSe_2$ flakes (see the Supporting Information for detailed description). As shown in **Figure 5**a ($MoSe_2$ on $Mo_{0.82}W_{0.18}Se_2$), the overlapping region of the two flakes formed a junction. The n-type behavior of the $MoSe_2$ and p-type behavior of the $Mo_{0.82}W_{0.18}Se_2$ in Figure 5a were verified by the transport curves shown in Figure 5b, indicating that the transfer and stacking process did not affect the individual electrical properties of each flake. The electrical properties of the junction area were measured using electrodes 2 and 3 as indicated in Figure 5a. The output curve at zero back-gate voltage shows an ideal current rectification behavior, with current only being able to pass through the device when the p-type $Mo_{0.82}W_{0.18}Se_2$ was forward-biased (Figure 5c). Since the individual flakes show very symmetrical output curves with respect to 0 V_{ds} (inset in Figure 5b), it was confirmed that the rectifying behavior originated from the p–n junction formed by the stacked monolayers of $MoSe_2$ on $Mo_{0.82}W_{0.18}Se_2$. The much decreased source-drain current in the junction could be due to the bubbles or wrinkles formed between layers during the wet transfer process.[41] However, despite the bubbles or wrinkles, the two stacked layers are well coupled as proven by low-frequency Raman spectra,[41] which leads to a p–n junction in the stacked monolayers. The characteristic of the p–n junction was also gate-tunable. The output current of the junction increased with increasing positive back-gate voltage (Figure 5d), and the transfer characteristic of the junction (inset in Figure 5d) was very similar to that measured for the n-type $MoSe_2$ (Figure 5b), indicating that the n-type $MoSe_2$ dominates the charge transport across the p–n junction. According to the above experimental data, since the source-drain current in monolayer p-type $Mo_{0.82}W_{0.18}Se_2$ is much higher (at about an order of magnitude) than that in monolayer n-type $MoSe_2$ at zero back-gate voltage (Figure 3) and the electron doping concentration in $MoSe_2$ is slightly lower than the hole doping in $Mo_{0.82}W_{0.18}Se_2$ according to the above experimental data, the charge transport across the p–n junction is dominated by the lower-doped component.[42]

In summary, a low-pressure CVD method was used to form uniform monolayer crystals of $MoSe_2$ and the isoelectronic substitutional alloy $Mo_{1-x}W_xSe_2$. Isoelectronic substitution resulted in highly uniform monolayer $Mo_{1-x}W_xSe_2$ alloys displaying greatly enhanced PL intensity without significant changes in

Adv. Mater. 2016,
DOI: 10.1002/adma.201601991

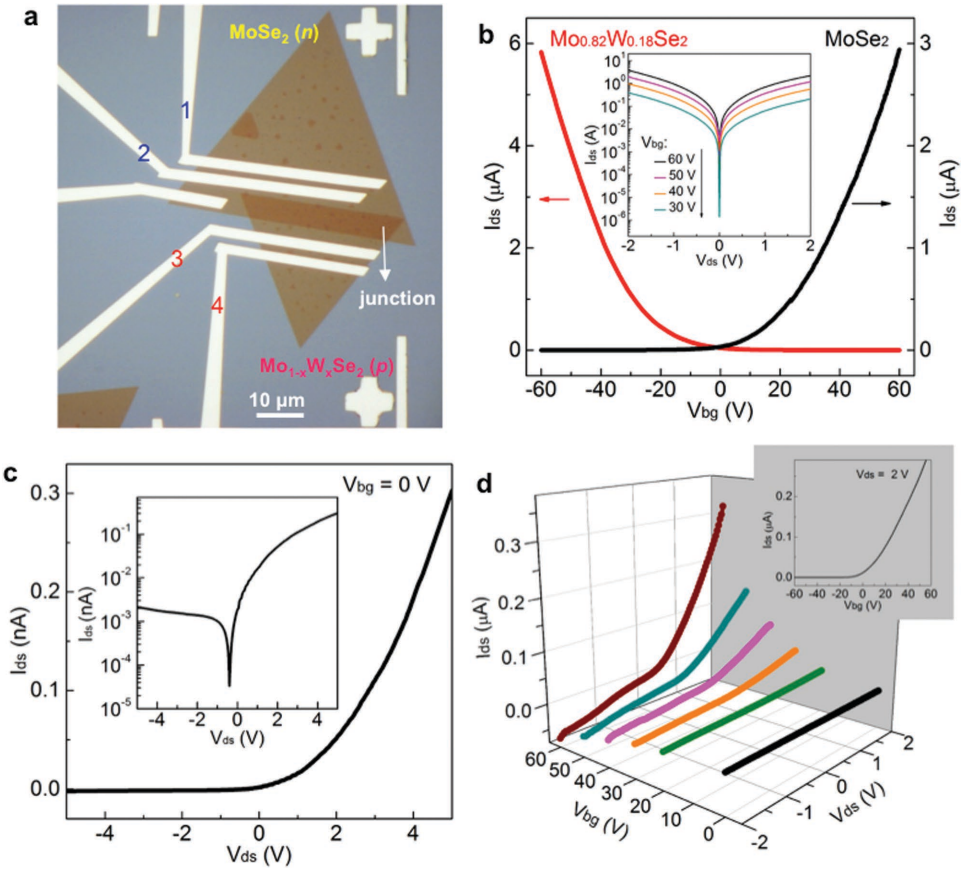

Figure 5. a) Optical micrograph of a monolayer $MoSe_2$ (upper flake) transferred and stacked onto a monolayer $Mo_{0.82}W_{0.18}Se_2$ (lower flake). The overlapping region of the two flakes forms a homojunction. Electrodes were deposited on both flakes (1 and 2 for $MoSe_2$, 3 and 4 for $Mo_{0.82}W_{0.18}Se_2$). The electrical properties of the junction were measured using electrode 2 and 3. b) Transfer (I_{ds}–V_{bg}) curves (at $V_{ds} = 2$ V) of the monolayer $MoSe_2$ and $Mo_{0.82}W_{0.18}Se_2$ in (a). Inset is the output (I_{ds}–V_{ds}) curves of the monolayer $MoSe_2$ on a logarithmic scale. c) Output curve (at $V_{bg} = 0$) of the junction. Inset is the same curve on a logarithmic scale. d) Output curves of the junction at different back-gate voltages. Inset is the transfer curve (at $V_{ds} = 2$ V) of the junction.

the optical bandgap. For the first time, carrier type modulation was demonstrated in 2D TMDs as n-type monolayer $MoSe_2$ was converted to nondegenerate p-type monolayer $Mo_{1-x}W_xSe_2$. Although the alloys are mesoscopically uniform in composition, "W-rich" and "Mo-rich" regions on atomic scale are observed, which could possibly be formed due to composition modulation or perturbation during the growth. The p-type conduction in monolayer $Mo_{1-x}W_xSe_2$ appears to originate from the upshift of the VBM toward the Fermi level at highly localized "W-rich" regions in the lattice. Atomically thin, vertically stacked p–n homojunctions fabricated by stacking the $Mo_{1-x}W_xSe_2$ and $MoSe_2$ monolayers displayed excellent current rectification and gate-tunable characteristics, indicating that isoelectronic alloying is a promising pathway to tune the electrical properties of 2D TMDs. The adjustable bottom-up synthesis of isoelectronically substituted uniform alloys demonstrated here appears highly promising as a method to not only enrich the variety of n- and p-type building blocks for 2D electronic and optoelectronic systems, but also to tunably modulate a variety of physical and chemical properties in layered and stacked systems.

Supporting Information

Supporting Information is available from the Wiley Online Library or from the author.

Acknowledgements

Special thanks goes to Mr. Ting Cao from Department of Physics at University of California Berkeley, Dr. Bing Huang from Beijing Computational Science Research Center, and Dr. Mina Yoon and Dr. Bobby G. Sumpter from Center for Nanophase Materials Sciences at Oak Ridge National Laboratory for their valuable discussion and advice on the electronic structure of monolayer $MoSe_2$ and $Mo_{1-x}W_xSe_2$. Synthesis science sponsored by the Materials Science and Engineering Division, Office of Basic Energy Sciences, U.S. Department of Energy. Materials characterization was conducted at the Center for Nanophase Materials Sciences, which is a DOE Office of Science User Facility.

Received: April 14, 2016
Revised: June 2, 2016
Published online:

[1] S. Z. Bulter, S. M. Hollen, L. Y. Cao, Y. Cui, J. A. Gupta, H. R. Gutiérrez, T. F. Heinz, S. S. Hong, J. X. Huang, A. F. Ismach, E. Johnston-Halperin, M. Kuno, V. V. Plashnitsa, R. D. Robinson, R. S. Ruoff, S. Salahuddin, J. Shan, L. Shi, M. G. Spencer, M. Terrones, W. Windl, J. E. Goldberger, *ACS Nano* **2013**, *7*, 2898.
[2] B. Radisavljevic, A. Radenovic, J. Brivio, V. Giacometti, A. Kis, *Nat. Nanotechnol.* **2011**, *6*, 147.
[3] O. Lopez-Sanchez, D. Lembke, M. Kayci, A. Radenovic, A. Kis, *Nat. Nanotechnol.* **2013**, *8*, 497.
[4] M. Bernardi, M. Palummo, J. C. Grossman, *Nano. Lett.* **2013**, *13*, 3664.
[5] S. Wu, S. Buckley, J. R. Schaibley, L. Feng, J. Yan, D. G. Mandrus, F. Hatami, W. Yao, J. Vučković, A. Majumdar, X. Xu, *Nature* **2015**, *520*, 69.
[6] Y. Gong, Z. Liu, A. R. Lupini, G. Shi, J. Lin, S. Najmaei, Z. Lin, A. L. Elìas, A. Berkdemir, G. You, H. Terrones, M. Terrones, R. Vajtai, S. T. Pantelides, S. J. Pennycook, J. Lou, W. Zhou, P. M. Ajayan, *Nano Lett.* **2014**, *14*, 442.
[7] H. Li, X. Duan, X. Wu, X. Zhuang, H. Zhou, Q. Zhang, X. Zhu, W. Hu, P. Ren, P. Guo, L. Ma, X. Fan, X. Wang, J. Xu, A. Pan, X. Duan, *J. Am. Chem. Soc.* **2014**, *136*, 3756.
[8] J. Mann, Q. Ma, P. M. Odenthal, M. Isarraraz, D. Le, E. Preciado, D. Barroso, K. Yamaguchi, G. von Son Palacio, A. Nguyen, T. Tran, M. Wurch, A. Nguyem, V. Klee, S. Bobek, D. Sun, T. F. Heinz, T. S. Rahman, R. Kawakami, L. Bartels, *Adv. Mater.* **2014**, *26*, 1399.
[9] S. Mouri, Y. Miyauchi, K. Matsuda, *Nano Lett.* **2013**, *13*, 5944.
[10] H. L. Zhuang, R. G. Hennig, *Chem. Mater.* **2013**, *25*, 3232.
[11] H. Yuan, M. S. Bahramy, K. Morimoto, S. Wu, K. Nomura, B.-J. Yang, H. Shimotani, R. Suzuki, M. Toh, C. Kloc, X. Xu, R. Arita, N. Nagaosa, Y. Iwasa, *Nat. Phys.* **2013**, *9*, 563.
[12] J. Suh, T.-E. Park, D.-Y. Lin, D. Fu, J. Park, H. J. Jung, Y. Chen, C. Ko, C. Jang, Y. Sun, R. Sinclair, J. Chang, S. Tongay, J. Wu, *Nano Lett.* **2014**, *14*, 6976.
[13] Y. Jin, D. H. Keum, S.-J. An, J. Kim, H. S. Lee, Y. H. Lee, *Adv. Mater.* **2015**, *27*, 5534.
[14] H.-M. Li, D. Lee, D. Qu, X. Liu, J. Ryu, A. Seabaugh, W. J. Yoo, *Nat. Commun.* **2015**, *6*, 6564.
[15] S. Tongay, J. Zhou, C. Ataca, J. Liu, J. S. Kang, T. S. Matthews, L. You, J. Li, J. C. Grossman, J. Wu, *Nano. Lett.* **2013**, *13*, 2831.
[16] H. Fang, M. Tosun, G. Seol, T. C. Chang, K. Takei, J. Guo, A. Javey, *Nano Lett.* **2015**, *13*, 1991.
[17] K. Zhang, S. Feng, J. Wang, A. Azcatl, N. Lu, R. Addou, N. Wang, C. Zhou, J. Lerach, V. Bojan, M. J. Kim, L.-Q. Chen, R. M. Wallace, M. Terrones, J. Zhu, J. A. Robinson, *Nano Lett.* **2015**, *15*, 6586.
[18] J.-G. Song, G. H. Ryu, S. J. Lee, S. Sim, C. W. Lee, T. Choi, H. Jung, Y. Kim, Z. Lee, J.-M. Myoung, C. Dussarrat, C. Lansalot-Matras, J. Park, H. Choi, H. Kim, *Nat. Commun.* **2015**, *6*, 7817.
[19] G. Wang, C. Robert, A. Suslu, B. Chen, S. Yang, S. Alamdari, I. C. Gerber, T. Amand, X. Marie, S. Tongay, B. Urbaszek, *Nat. Commun.* **2015**, *6*, 10110.
[20] D. Dolui, I. Rungger, C. D. Pemmaraju, S. Sanvito, *Phys. Rev. B.* **2013**, *88*, 075420.
[21] Z. Xu, J. Zhang, H. Duan, Z. Zhang, Q. Zhu, X. Xu, *J. Semicond.* **2009**, *30*, 123003.
[22] W. Liu, N. Chen, *J. Cryt. Growth* **1995**, *154*, 19.
[23] S. Zheng, L. Sun, T. Yin, A. M. Dubrovkin, F. Liu, Z. Liu, Z. Shen, H. Fan, *Appl. Phys. Lett.* **2015**, *106*, 063113.
[24] D. O. Dumcenco, H. Kobayashi, Z. Liu, Y.-S. Huang, K. Suenaga, *Nat. Commun.* **2013**, *4*, 1351.
[25] S. Yoshida, Y. Kobayashi, R. Sakurada, S. Mori, Y. Miyata, H. Mogi, T. Koyama, O. Takeuchi, H. Shigekawa, *Sci. Rep.* **2015**, *5*, 14808.
[26] X. Wang, Y. Gong, G Shi, W. L. Chow, K. Keyshar, G. Ye, R. Vajtai, J. Lou, Z. Liu, E. Ringe, B. K. Tay, P. M. Ajayan, *ACS Nano* **2014**, *8*, 5125.
[27] H. Zhou, C. Wang, J. C. Shaw, R. Cheng, Y. Chen, X. Huang, Y. Liu, N. O. Weiss, Z. Lin, Y. Huang, X. Duan, *Nano Lett.* **2014**, *15*, 709.
[28] R. Cheng, D. Li, H. Zhou, C. Wang, A. Yin, S. Jiang, Y. Liu, Y. Chen, Y. Huang, X. Duan, *Nano Lett.* **2014**, *14*, 5590.
[29] W. Liu, J. Kang, D. Sarkar, Y. Khatami, D. Jena, K. Banerjee, *Nano Lett.* **2013**, *13*, 1983.
[30] B. Huang, M. Yoon, B. G. Sumpter, S.-H. Wei, F. Liu, *Phys. Rev. Lett.* **2015**, *115*, 126806.
[31] A. Kutana, E. S. Penev, B. I. Yakobson, *Nanoscale* **2014**, *6*, 5820.
[32] S. Tongay, D. S. Narang, J. Kang, W. Fan, C. Ko, A. V. Luce, K. X. Wang, J. Suh, K. D. Patel, V. M. Pathak, J. Li, J. Wu, *Appl. Phys. Lett.* **2014**, *104*, 012101.
[33] H. W. Shiu, L. Y. Chang, K.-H. Lee, H.-Y. Chen, S. Gwo, C.-H. Chen, *Appl. Phys. Lett.* **2013**, *103*, 081604.
[34] B.-J. Hwang, L. S. Sarma, J.-M. Chen, C.-H. Chen, S.-C. Shih, G.-R. Wang, D.-G. Liu, J.-F. Lee, M.-T. Tang, *J. Am. Chem. Soc.* **2005**, *127*, 11140.
[35] K. Dolui, I. Rungger, S. Sanvito, *Phys. Rev. B* **2013**, *87*, 165402.
[36] C. Ataca, S. Ciraci, *J. Phys. Chem. C* **2011**, *115*, 13303.
[37] B. Chakraborty, A. Bera, D. V. S. Muthu, S. Bhowmick, U. V. Waghmare, A. K. Sood, *Phys. Rev. B* **2012**, *85*, 161403(R).
[38] J. Xi, T. Zhao, D. Wang, Z. Shuai, *J. Phys. Chem. Lett.* **2014**, *5*, 285.
[39] C.-S. Kim, S. H. Cheong, D. S. Kang, J. Y. Kim, C.-H. Hong, E.-K. Suh, H. J. Lee, K.-H. Cho, I. Adesida, *J. Korean Phys. Soc.* **2004**, *45*, 1391.
[40] M. M. Ugeda, A. J. Bradley, S.-F. Shi, F. H. da Jornada, Y. Zhang, D. Y. Qiu, W. Ruan, S.-K. Mo, Z. Hussain, Z.-X. Shen, F. Wang, S. G. Louie, M. F. Crommie, *Nat. Mater.* **2014**, *13*, 1091.
[41] A. A. Puretzky, L. Liang, X. Li, K. Xiao, B. G. Sumpter, V. Meunier, D. B. Geohegan, *ACS Nano* **2016**, *10*, 2736.
[42] X. Duan, C. Wang, J. C. Shaw, R. Cheng, Y. Chen, H. Li, X. Wu, Y. Tang, Q. Zhang, A. Pan, J. Jiang, R. Yu, Y. Huang, X. Duan, *Nat. Nanotechnol.* **2014**, *9*, 1024.

Adv. Mater. **2016**,
DOI: 10.1002/adma.201601991